Applied Physics B (2017) 123:282
https://doi.org/10.1007/s00340-017-6858-9

Applied Physics B
Lasers and Optics

Characteristics of hierarchical micro/nano surface structure formation generated by picosecond laser processing in water and air

Fatema H. Rajab[1,2] · David Whitehead[1] · Zhu Liu[1,3] · Lin Li[1]

Received: 29 May 2017 / Accepted: 5 November 2017 / Published online: 13 November 2017

Abstract
Laser surface texturing or micro/nano surface structuring in the air has been extensively studied. However, until now, there are very few studies on the characteristics of laser-textured surfaces in water, and there was no reported work on picosecond laser surface micro/nano-structuring in water. In this work, the surface properties of picosecond laser surface texturing in water and air were analysed and compared. 316L stainless steel substrates were textured using a picosecond laser. The surface morphology and the chemical composition were characterised using Philips XL30 FEG-SEM, EDX and confocal laser microscopy. The wettability of the textured surfaces was determined using a contact angle analyser FTA 188. Results showed that a variety of hierarchical micro/nano surface patterns could be controlled by a suitable adjustment of laser parameters. Not only surface morphology but also remarkable differences in wettability, optical reflectivity and surface oxygen content were observed for different types of surface textures produced by laser surface texture in water and air. The possible mechanisms of the changes in the behaviour of laser-textured surfaces are discussed.

1 Introduction

Changing surface properties by micro/nano texturing or patterning has been widely investigated for their applications in many fields. For example, it has been used for modifying the optical properties (absorption, reflection, colour) of surfaces which are used in photosensors, enhanced Raman imaging [1, 2] and improved energy conversion efficiency in photovoltaics. It has also been used for altering surface's wettability, which is beneficial in applications including self-cleaning, anti-icing, fluidic control and drag reduction [3–7]. It has been used for modifying the surfaces for biological applications for controlling cell and bacteria behaviour [8–14]. Different methods, such as plasma treatment, chemical-assisted etching, electrochemical anodization and moulding, have been used to fabricate these surfaces. However, these techniques are complicated, time-consuming and often require vacuum conditions. Therefore, the demand for simple, flexible and more environmentally friendly techniques such laser technologies has been increased [15].

Laser surface texturing or structuring had been mostly carried out using nanosecond pulsed lasers due to their high average power, low cost and high productivity. Recently, ultrafast lasers (ps and fs pulses) have been increasingly investigated for surface micro/nano texturing [2–5]. The advantages of using ultrashort laser pulses include better process control and suitability for patterning transparent materials [6, 7]. These advantages are related to the way the laser energy is deposited in the material and material responses. The mechanism of material removal in ultrafast laser processing is different from that of longer pulses. For ultrashort pulsed laser surface texturing, vaporisation and plasma formation dominate the process while for nanosecond pulses, melting, resolidification and splashing dominate [16]. It is known that a higher throughput microscale structure formation can be achieved using nanosecond laser processing based on high fluence laser melting and resolidification. Ultrafast lasers (i.e. picosecond and femtosecond pulsed lasers) are normally good

✉ Fatema H. Rajab
fatema.rajab@postgrad.manchester.ac.uk;
fatemarajab83@gmail.com

[1] Laser Processing Research Centre, School of Mechanical, Aerospace and Civil Engineering, The University of Manchester, Manchester M13 9PL, UK

[2] College of Engineering, Al-Nahrain University, Baghdad, Iraq

[3] School of Materials, The University of Manchester, Manchester M13 9PL, UK

at inducing nano-structures and hybrid nano/micro structures. With the development of high repetition rate and high power ps lasers, high ablation rates can be achieved while producing micro/nano surface structures of good quality [17].

During laser surface structuring in the air, oxidation, coarse structures, vapour deposition and spatter formation are often seen. Some of these such as oxidation would be much less for laser processing in water [18]. Different techniques of laser processing in water were conducted by immersing the samples in water [19, 20], flow of water during process [18] and drop of water using a syringe [21].

The relationships between processing parameters such as laser fluence, scanning speed, focused spot size, the number of pulses, processing environment and material properties during laser processing greatly affect the quality and final properties of treated surfaces [22]. Different micro and nano-structures have been induced on metal surfaces depending on the laser processing parameters. These structures can take the form of periodic ripple structures [23–27], grooves [27–29], spikes, bumps [11, 13, 30, 31], holes or pores [27, 29, 32], cauliflower-like structures [33] and conical structure [7, 34–38]. By optimising one or several processing parameters, a wide range of micro/nano-structures can be achieved.

Stainless steel is a useful alloy used in many scientific and manufacturing areas. Controlling its surface micro- and nano-structures can provide additional beneficial properties. So far, there had been a few research papers reporting on laser surface texturing in water [20, 39–41]. However, no work was reported on picosecond laser surface micro/nano-structuring or texturing in water and how it was different from texturing in the air. Therefore, in this work, a series of laser texturing experiments were conducted to fabricate micro- and nano-structures on the 316L stainless steel sheets using picosecond laser processing in air and water. The influence of scanning speed and scanning pass times on the morphology, wettability, light reflectivity and surface oxygen contents was investigated in detail.

2 Experimental procedure

2.1 Experimental sample preparation

AISI 316L stainless sheets with dimensions of 10 mm × 10 mm × 0.7 mm (length x width x thickness) were used in this work. Before the laser processing, the samples were cleaned ultrasonically with acetone followed by ethanol, then de-Ionized water (DIW) rinsing for 10 min, respectively.

2.2 Laser surface structuring

A picosecond (Edgewave, Nd: YVO_4, laser parameters: wavelength $\lambda = 1064$ nm, repetition rate = 103 kHz, focused beam spot size $D = 125$ µm, pulse duration = 10 ps and laser fluence = 0.177 J/cm^2) was used to irradiate the stainless steel sheets. Laser texturing was performed in a raster scan manner (parallel lines) in air and water, respectively, to study the effect of scanning speed and scanning passes on micro/nano-structure formation, wettability, optical reflectivity and surface oxygen content. The laser beams were directed to a set of x–y galvo scanning mirrors then focused onto the sample by a theta flat field lens with a focal length $F = 245$ mm. The scanning was performed with a hatch distance (line to line distance) of 10 µm, at various scanning speeds (1, 10, 50, 500 and 1000 mm/s) and number of scanning passes (1, 10, 50 and 100 passes). The reason that 10 µm hatch distance was chosen was to increase the overlapping and study the effect of scanning speed and scanning times on micro- and nano-structures. The experiments were performed in air at atmospheric pressure and under de-Ionized water (DIW). The level of water was 1 mm above the sample. The schematic arrangement of the laser texturing experiments is shown in Fig. 1.

2.3 Sample characterisation

After the laser surface structuring, the samples were cleaned ultrasonically with ethanol then ablated debris or contamination were removed with compressed air. For characterising the surface morphology and the surface oxygen contents, scanning electron microscopy (Philips XL30 FEG-SEM) incorporating with energy dispersive analysis by X-ray (EDX) was used. The roughness of the surface was measured

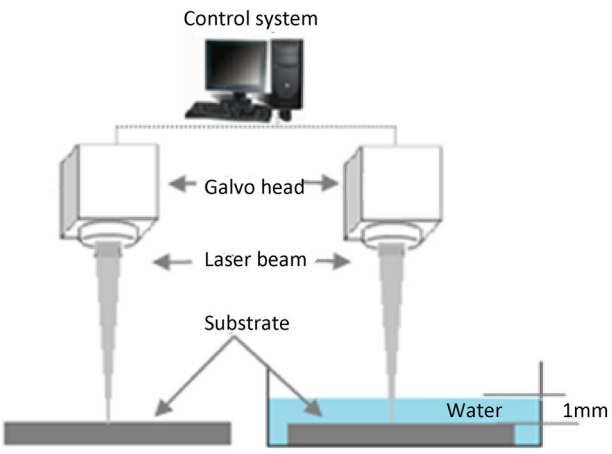

Fig. 1 Experimental scheme of laser-textured surface in air (left) and water (right)

using confocal laser microscopy (CLM) with an objective lens of 150 × magnification.

2.4 Wettability investigation

To investigate the effects of the laser irradiation on the wettability characteristics of the samples, a water drop sessile method using a contact angle analyser FTA 188 was used. Briefly, the samples were divided into two groups. The first one was immersed into a 1% hetadecafluoro-1,1,2,2-tetrahydro-decyl-1-trimethoxysilane ($CF_3(CF_2)_7(CH_2)_2Si(OCH_3)_3$ methanol solution for 2 h followed by washing in ethanol and drying in an oven at 80 °C for 30 min [6]. This was performed to reduce the surface tension and eliminate the effect of laser-generated surface chemistry change and study the effect of surface geometry. The second group of samples was left without further treatment. Then, 5 µl droplets of DI water were allowed to contact the surface. The average contact angles of three measurements were recorded.

2.5 Optical reflectivity measurement

To measure the light reflectance of the samples, UV–VIS spectroscopy (Analytik Jena Specord 250) was used. The spectral reflectance of laser-treated samples as well as the as received (untreated) one was measured over a wavelength range of 350–1100 nm.

3 Results

3.1 Surface morphology

The threshold fluence was determined from plots of depth per pulse against the laser fluence, to be 0.14 J/cm^2 and 0.11 J/cm^2, in air and water, respectively. In this work, a laser fluence of 0.177 J/cm^2 at different scanning speeds and multiple passes was used. Typical surface morphologies of the picosecond laser surface texturing in the air are shown in Fig. 2. It can be seen that, at a high laser scanning speed of 1000 mm/s, the main structure was Laser-Induced Periodic Surface Structures (LIPSS) decorated with fine rims. The periodicity of the ripples was measured to be 0.54 ± 0.09 µm, while the size of the nano-rims was 0.11 ± 0.01 µm. The size of the ripples was increased with decreasing scanning speed. At a 50 mm/s scanning speed, the induced structure was a combination of ripples (with a periodicity of 0.72 ± 0.2 µm) and small holes (typical diameters of 0.8 ± 0.04 µm). At a very low scanning speed of 10 mm/s, the structure was dominated by micro-cones of 5.6 ± 1.3 µm width decorated with nanoparticles of 40–150 nm in size. The width of the microgrooves between the cones was 0.8 ± 0.34 µm. Figure 3 shows the variation of micro/nano-structures with the laser scanning speed following the picosecond laser surface texturing in water. The laser was linearly polarised, and the scanning direction was perpendicular to the laser polarisation direction. Nano protrusions and particles with diameters of 10–150 nm and nano-rims of 40 ± 10 nm were seen at the high scanning speed (1000 mm/s). The LIPSS induced at 50 mm/s were irregular with a typical size of 300 ± 150 nm. These ripples were decorated with nanoparticles with diameters of 30–130 nm. There were also nano holes with diameters of 537 ± 100 nm. Regular fine ripples with a width of 261 ± 90 nm decorated with nanoparticles of 70 ± 30 nm in diameter were induced at a very low scanning speed (10 mm/s). Using a very small hatch distance (10 µm) with a low scanning speed (1 mm/s), the laser-textured area in the air showed a pillow likes structure with clear grooves while in water, an LIPSS structure was dominant with a periodicity of 513 ± 80.5 nm. This LIPSS was separated with holes within grooves with the size of 790 ± 190 nm.

Surface structures generated in water were smaller in feature sizes compared with that generated in air. Figure 4 shows the effect of changing the scanning speed and number of scan passes on surface roughness. It is clear that the surface roughness was

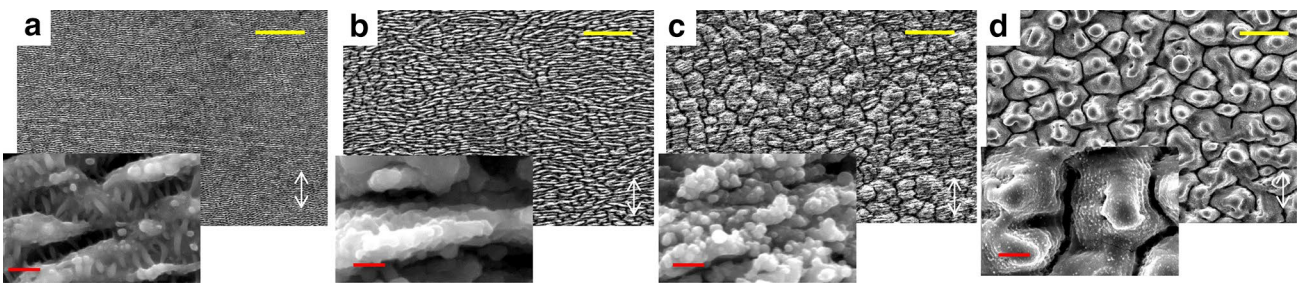

Fig. 2 Surface structure characteristics of ps laser surface textured samples processed in air using: **a** 1000 mm/s (92% pulse overlapping), **b** 50 mm/s (99.6% pulse overlapping), **c** 10 mm/s (99.9% pulse overlapping) and **d** 1 mm/s (99.99% pulse overlapping) for 1 scanning pass, scale bar is 20 µm (yellow) and 500 nm (red). White arrows indicate the coinciding direction of the polarization vector of the laser field

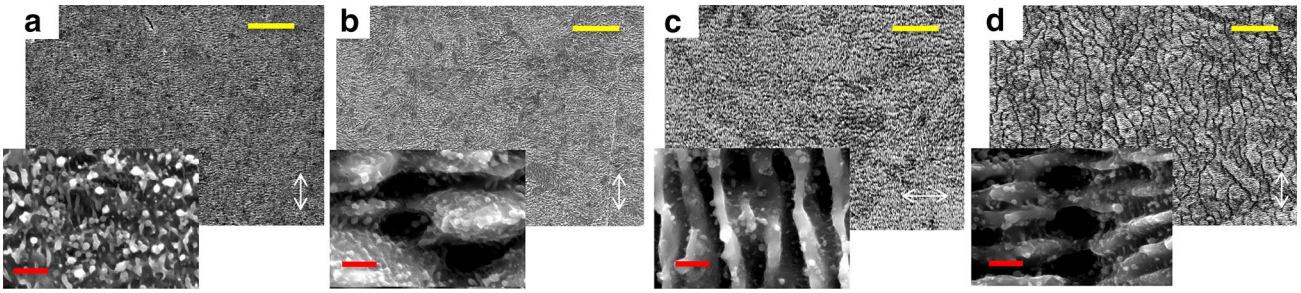

Fig. 3 Surface structure characteristics of ps laser surface textured samples in water using: **a** 1000 mm/s (92% pulse overlapping), **b** 50 mm/s (99.6% pulse overlapping), **c** 10 mm/s (99.9% pulse overlapping) and **d** 1 mm/s (99.99% pulse overlapping) for 1 scanning pass, scale bar is 20 µm (yellow) and 500 nm (red).White arrows indicate the coinciding direction of the polarization vector of the laser field

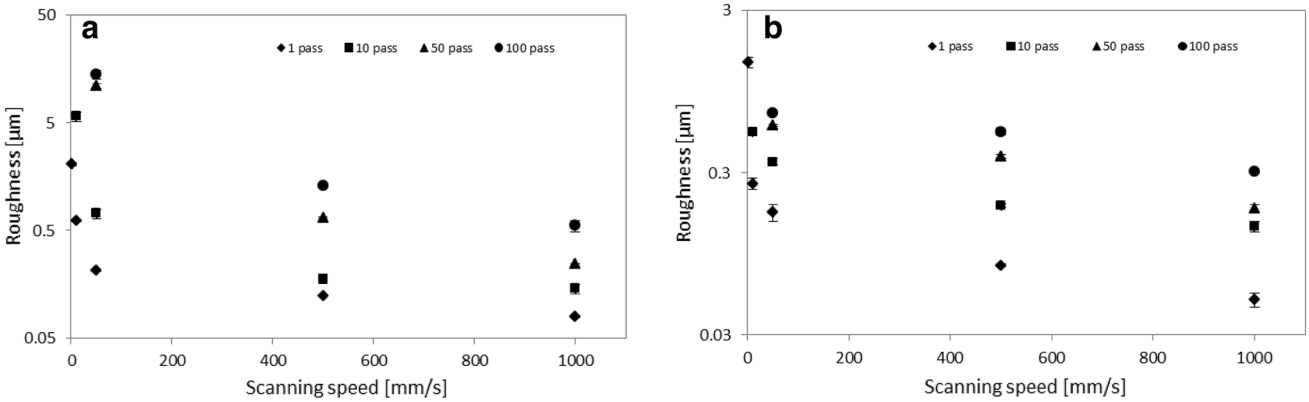

Fig. 4 The change of roughness of surfaces textured in air and water as a function of laser scanning speed and scanning pass using Ps laser surface texturing in air (**a**) and water (**b**)

decreased with increasing scanning speed and was increased with increasing scanning passes at a specific speed. The roughness of surfaces textured in the air was much higher than that achieved in water. For example, at a 50 mm/s scanning speed and 100 scanning passes, the roughness, R_a, in the air was 14 ± 2.6 µm whereas it was just 0.7 ± 0.1 µm in water.

3.2 Surface chemistry

The energy dispersive X-ray spectroscopy (EDXs) analysis result is shown in Fig. 5 for laser surface texturing using the ps laser in air and water. An increase in the surface oxygen content was observed in all the processing conditions. Indeed, the oxygen level increased with increasing number of scanning passes at a specific scanning speed and with decreasing scanning speed. It was also noticed that the oxygen percentage of surfaces treated in the air was significantly higher than that in water. For example, at the 1 mm/s scanning speed, the percentage of the oxygen was 17% in air and less than 2% in water. It was also noticed, as shown in Fig. 5, that with increasing the roughness the oxygen percentage was also increased.

3.3 Surface wettability

In this work, the wettability of various surface micro/nano-structures was examined for samples with and without a chemical coating. Most of the published work was focused on studying the wettability of metal surfaces processed in air. In this work, the effect of air and underwater ps laser-generated surface micro/nano-structures in changing the stainless steel (SS) wettability was investigated. For wettability tests, two sets of samples were prepared. The first set of surfaces was treated chemically after laser processing to reduce surface tension and to provide a common surface chemistry for the examination of the surface structure effect only. Figure 6 presents the change of surface wettability as a function of surface roughness in air and water, respectively. When processing in the air (Fig. 6a), it is clear that the contact angle increased with increasing surface roughness in all cases. The surface was superhydrophobic with maximum contact angles (CAs) around 160°. However, for the surfaces treated in water (Fig. 6b), the wettability was slightly lower than that recorded in the air. The maximum measured CA in water was ~150°. The minimum CA in the case of ps surface structuring in air

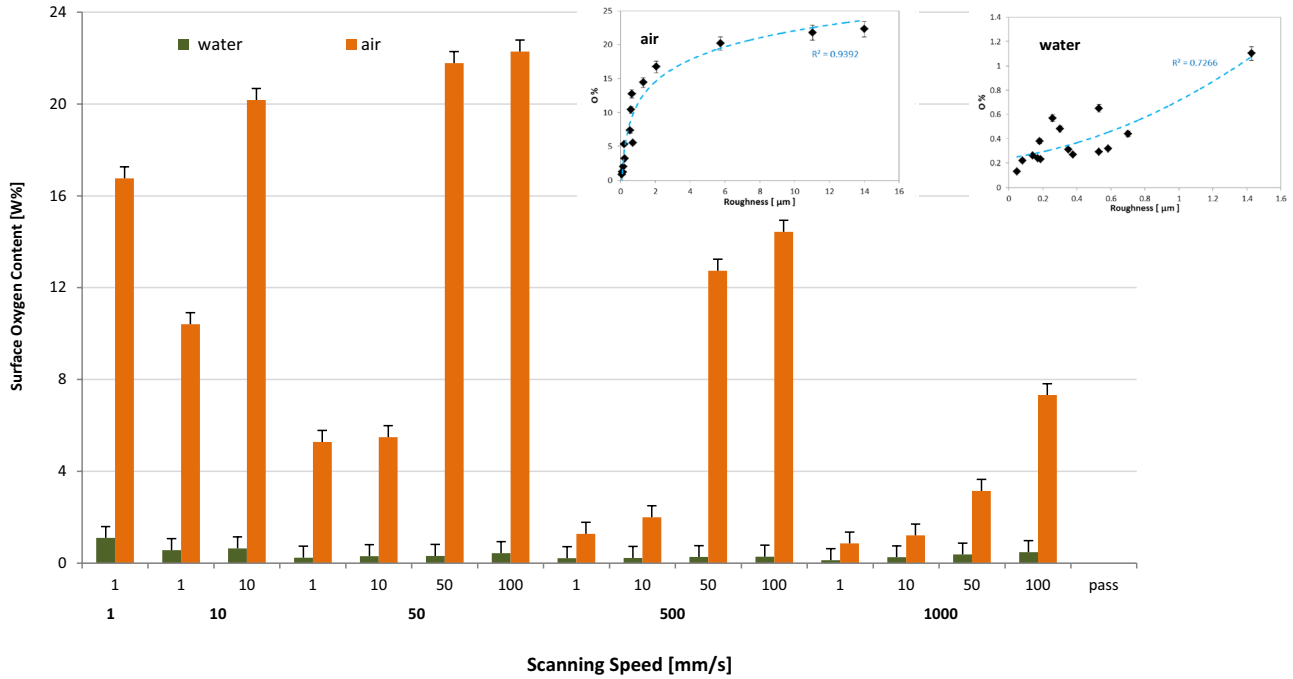

Fig. 5 Oxygen content on the surface of laser irradiated 316L SS after Ps laser surface texturing

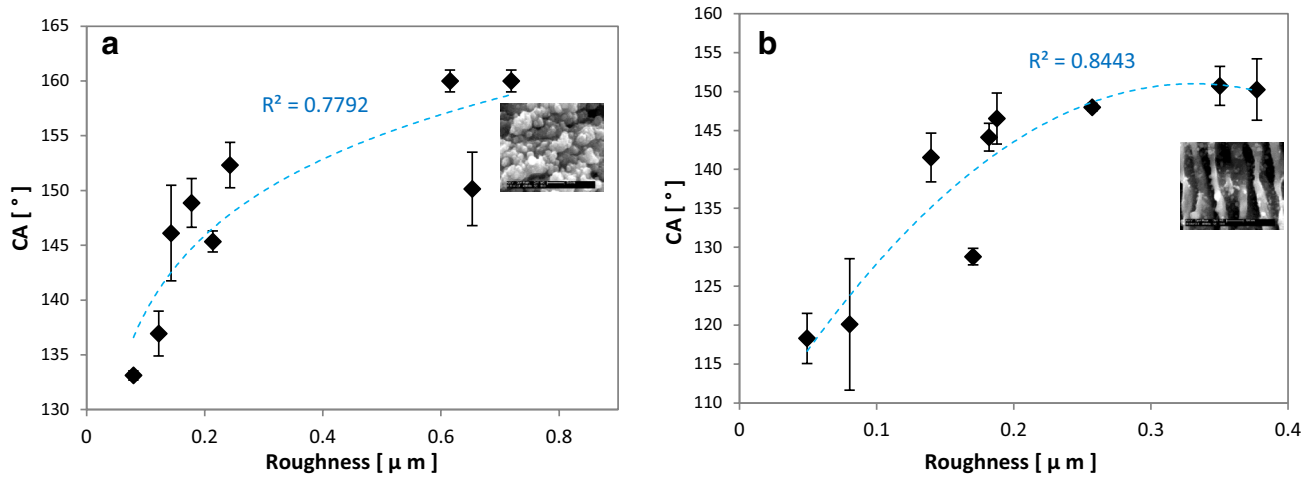

Fig. 6 Contact angle as a function of surface roughness with reducing the surface energy for ps textured the surface in the air (**a**) and water (**b**)

and water was ~130° and ~120°, respectively. Generally, the wettability of surfaces treated in water was higher than that treated in the air.

The second set of samples was examined without any subsequent chemical treatment, and their wettability was investigated one month after the laser surface texturing. The trend of the wettability was opposite to that achieved for samples with chemical treatment (Fig. 7). The results showed that the wettability was increased with increasing the surface roughness in all cases. However, it was noticed that the water contact angles (CA) in the air were also higher than those processed in water. The maximum CA of the surfaces treated using the ps laser in the air was ~98°, whereas it was around 87° in water. The decrease in the CA was not much and the measured minimum CAs were 75° in the air and 65° in water. Therefore, it can be said that without the chemical treatment, the main factors affecting the surface wettability were the surface roughness and surface chemistry.

The surface free energy data for the surfaces of higher contact angles obtained are listed in Table 1. The surface free energy of the laser-textured surfaces was obtained by measuring the contact angle of water, formamide and

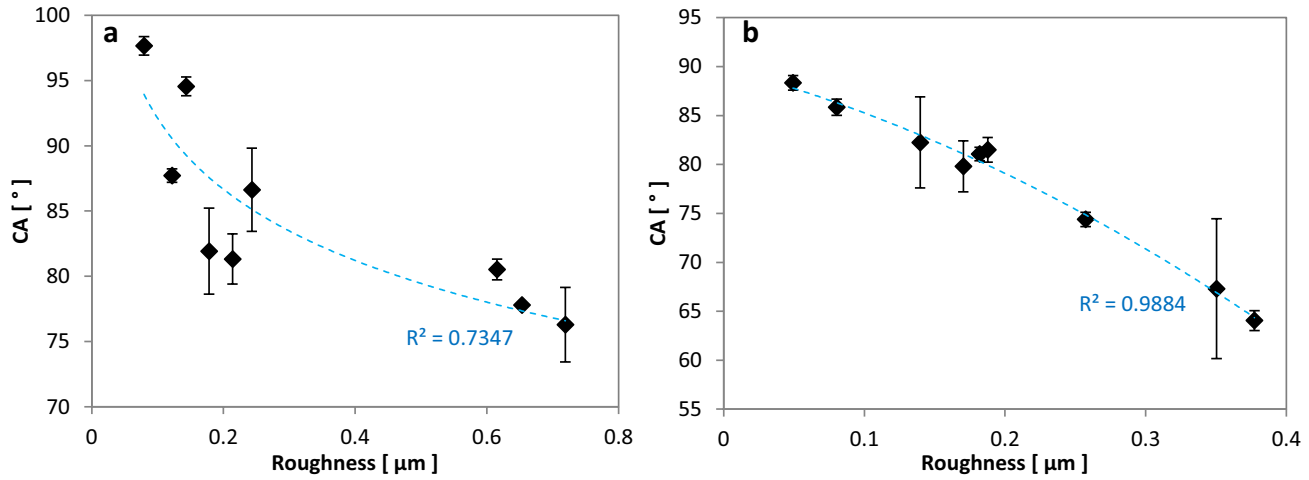

Fig. 7 Contact angle as a function of surface roughness without chemical treatment of reducing the surface energy for Ps treated the surface in the air (**a**) and water (**b**) one month after laser treatment

Table 1 Surface energy mJ/m^2 for laser-treated surface before and after chemical treatment for the surfaces treated using 10 mm/s, one pass. (RST) surface after chemical treatment

Surface	ΔG_{iwi}	γ_s	γ_s^{LW}	γ_s^{AB}	γ_s^+	γ_s^-
Ps RST	− 67.87	6.75	2.91	3.83	0.96	3.84
PS	− 26.38	25.20	23.63	1.57	0.04	13.61

α-bromonaphthalene. Then, Van Oss et al. 's approach was used as [43, 44]:

$$(1+\cos\theta)^{TOT}_{\gamma_L} = 2\left(\sqrt{\gamma_S^{LW}\gamma_L^{LW}} + \sqrt{\gamma_S^{+}\gamma_L^{-}} + \sqrt{\gamma_S^{-}\gamma_L^{-}}\right) \quad (1)$$

where θ is the contact angle, and $\gamma^{TOT} = \gamma^{LW} + \gamma^{AB}$. γ^{LW}, γ^+ and γ^- are, respectively, the Lifshitz–van der Waals component of the surface free energy, the electron acceptor and donor parameters of the Lewis acid–base component γ^{AB}, where $\gamma^{AB} = 2\sqrt{\gamma^+\gamma^-}$. Using three different liquids with their known surface tension components and their measured contact angles, a linear set of equations was obtained from Eq. 1 (one equation of each liquid). This set of equations was solved to obtain solid surface energy components. Then, the hydrophobicity of the surface was calculated as:

$$\Delta G_{iwi} = -2\left(\sqrt{\gamma_S^{LW}} - \sqrt{\gamma_L^{LW}}\right)^2 + 4\left(\sqrt{\gamma_S^{+}\gamma_W^{-}} + \sqrt{\gamma_S^{-}\gamma_W^{-}} - \sqrt{\gamma_S^{+}\gamma_S^{-}} - \sqrt{\gamma_W^{+}\gamma_W^{-}}\right) \quad (2)$$

It is clear from Table 1 that the surfaces textured using the ps laser after chemical treating was of higher hydrophobicity ($\Delta G_{iwi} = 67.87 mJ/m^2$) and lower surface tensions (γ_s, γ_s^{LW}, and γ_s^-). However, without the chemical treatment, the same surface presented higher values of surface tensions (γ_s, γ_s^{LW}, and γ_s^-), which reflects the surface energy.

3.4 Optical reflectivity

After the laser surface structuring, it was noticed that the reflectivity of the surface was changed as shown in Fig. 8. The reflectivity was investigated for different laser scanning speeds with one pass. It is clear that the reflectivity of SS 316L was decreased after the laser surface structuring. Indeed, the reflectivity of surfaces prepared in the air was low compared with that prepared underwater. The reflectivity of untreated SS was around 60% while it was decreased to less than 5 and 20% for laser-treated surfaces in air and water, respectively.

4 Discussion

The interaction mechanisms of the long and short pulse laser surface structuring are different. The laser–material interaction process is generally described by three main steps: surface absorption of laser energy, energy redistribution by electron–photon coupling and thermally induced melting, and ablation of the substrate [24]. The thermal diffusion length can be calculated by $\sqrt{D\tau}$, where D and τ are, respectively,

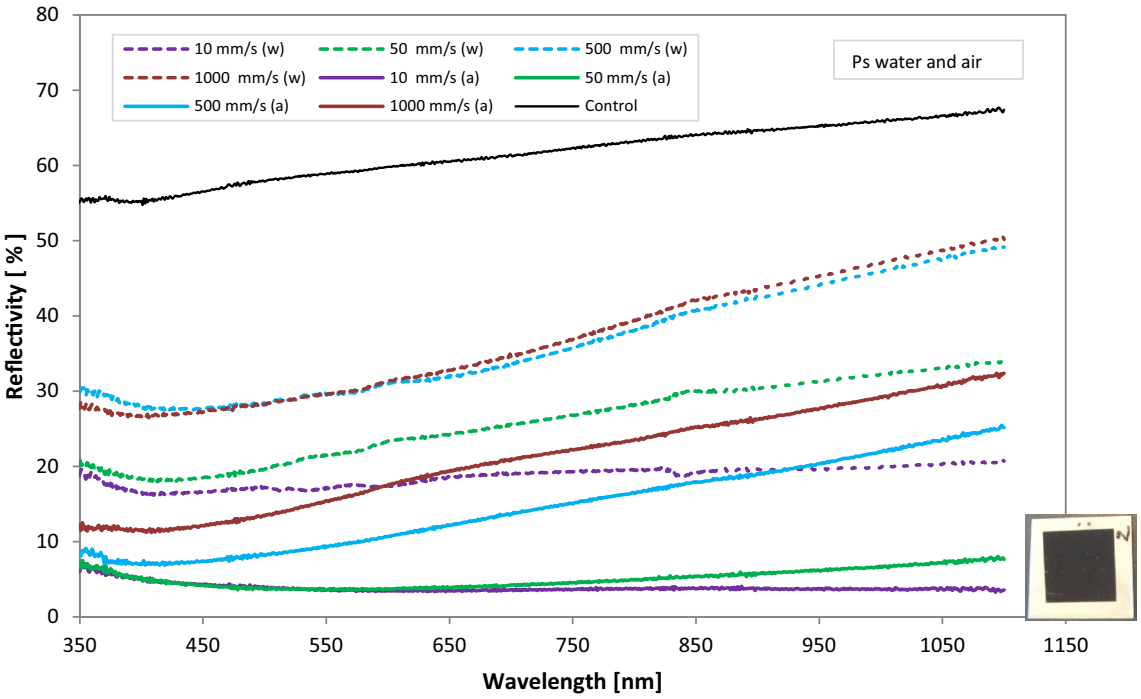

Fig. 8 Reflectivity changes for surfaces prepared using the ps laser processing in water and air

the thermal diffusivity = $K/\varrho c_p$ (with K being thermal conductivity, ϱ the mass density and c_p the specific heat) and pulse duration. Therefore, shorter pulse duration would result in less thermal effect, a smaller heat affected zone (HAZ) and more precise material removal. Using ultrashort pulsed lasers, the thermal effect could be reduced to the optical penetration depth with negligible thermal effects [42]. The optical penetration depth equals to $1/\alpha$, where α is the absorption coefficient. In this work, and using the thermal properties of SS 316 ($\varrho = 7950\text{kg/m}^3$, $C_p 470\text{J/kgk}$ and $K = 20\text{w/mk}$), the thermal and optical penetration depth was, respectively, 7 and 18 nm for the 10 ps laser pulse. The thermal penetration depth was shortened to less than the optical penetration depth. The thermalization time of electron–phonon coupling is in the range of 1–5 ps [43]. As the used pulse duration was 10 ps, it was higher than the thermalization time. The threshold fluence was estimated to be 0.14 J/cm^2 (air) and 0.11 J/cm^2 (water). Compared with the laser fluence used in this study (0.177 J/cm^2), they are lower. Therefore, it can be said that, for one pulse, the pulse energy was enough to initiate modification/ablation of the steel surface. The ablated volume can be estimated as [44]:

$$V_{\text{ab}} = (1 - R)Ep/\left(n_0 E_{\text{at}}\right)/N_{\text{a}} \tag{3}$$

where N_{a} is the Avogadro number, E_{at} is the molar enthalpy of atomization, $n_0 = \varrho N_{\text{a}}/M$ is the atomic number density of material (with ϱ being the mass density, and M the molar mass), and $(1 - R)Ep$ is the absorbed fraction of the pulse energy The ablated volume of the substrate at the incident pulse energy and using SS parameters ($\varrho = 7950$ (kg/m^3), $E_{\text{at}} = 414.2$ kJ/mol, $R = 50\%$ at 1.064 µm) was 183.59 nm^3.

As the process was performed line by line scanning with a specific line to line distance (10 µm), the generation of different micro/nano-structures on SS was affected by pulse/line overlapping and the number of pulses per spot. Pulse overlapping in the direction of scanning can be estimated as $(1 - \Delta x/\text{spot size}) \times 100$, where Δx = speed/repition rate and line overlapping in the direction perpendicular to the scanning direction can be estimated as $(1 - \Delta z/\text{spotsize}) \times 100$, where Δz is hatch distance [30]. In this work, the number of pulses ranged from 13 to 12875 by changing the scanning speed from 1000 mm/s to 1 mm/s to reach 1300 after 100 passes using 1000 mm/s. Indeed, the pulse overlapping was increased from 92% to 99.99% by decreasing the scanning speed from 1000 mm/s to 1 mm/s. Line overlapping, on the other hand, was 92%. In this work, the effect of changing the scanning speed and number of scanning passes on different structure formations was examined. The focused spot size was 125 µm and the applied hatch distance was 10 µm. For the ps laser interaction with the material, the material cannot evaporate continuously; thus, it is transferred into a state of overheated liquid, due to the short interaction time. This leads to a high pressure mixture of liquid droplets and vapour expanding rapidly ending with phase explosion at the high laser density [16]. In this work, different surface micro/nano-structures were achieved by manipulating the scanning

parameters. The first geometry includes nano-structures like rims, ripples, and protrusions. It is well known that the ripple formation depends on the laser fluence and it can be formed at low fluences with a lower scanning speed or at high fluences with high scanning speeds [45]. In this work, the ripples were formed on both samples treated at a high scanning speed (1000 mm/s) in air and water. The interference of incident and scattered laser irradiation or excited surface waves would be one of the mechanisms of ripple formation, which depends on the roughness of the surfaces [45]. The ripples were formed in the direction of scanning and it was noticed that nano rims with a dimension of 107 ± 10 nm intersected the ripples and perpendicular to the scanning direction were formed (Fig. 2a). With decreasing scanning speeds, some holes were clearer. The formation of these holes may be explained by the mechanism of rapid cooling and solidification of overheated liquid expulsion [16, 29]. These holes were also noticed on the surfaces treated in the water environment. With decreasing the scanning speeds, dual micro/nano scale structures were achieved including pillow or conical-like structures decorated with nano-structures. The formation of these structures was related to the high number of pulses per spot with an increase and accumulation of laser energy to increase the ablation rate. These structures were formed at low scanning speeds for one scanning pass (Fig. 2c) or multiple scanning passes (Fig. 9). In both cases, the overlapping of laser pulses was very high in both directions resulting in a considerable high amount of laser energy deposited in a specific small surface area. Following the first pulse, re-solidified particles can form. The fluence of the next pulse and next pass may enhance the vapour deposition. Due to a rougher surface, the beam absorption was increased, causing enlarged energy deposition due to multiple laser beam absorption. Then, local overheating of the material may occur and, in addition to material ablation, enhanced material melting can potentially take place. The rounded structure was covered by submicron features which is a result of sintering of ablated materials together forming these particles [35] (Fig. 9).

Unlike laser surface structuring in air, the results of underwater experiments almost uniformly modified the surfaces and free of redeposited particles. This is related to the fact that the derbies could be carried away due to the thermal convection of liquid or with the liquid movements induced by generated bubbles. Bubble formation and nanoparticles are specific phenomena that exist in the laser material processing in the presence of water (see Fig. 10). The change of water colour and its absorbance during processing indicates the generation of nanoparticles (see Fig. 10a). Due to water movement, these nano particles did not redeposit on the surface. This interprets the smoothness of structures induced in water [20, 46]. The absorbed energy on the target results in heating the material and forming a plume that expands in water and transfers its energy to thermal energy to the water by a thermodynamic process. The transferring of heat from the plume to water results in slowing down the ablated material velocity which leads to bubble formation [47]. Indeed, during the process, the temperature of the water was increased. For example, for the surface treated using 10 mm/s, the water temperature was increased from room temperature to 35°. Therefore, it can be said that the water also works as a cooling system which makes the generated surfaces finer. It has been reported that, in laser ablation in water, the generated bubble works as a negative lens that diverges and distorts the probe beam resulting in the reduction of the ablated material and enhancing the beam transmission as it has a hemispherical shape of refractive index of lower gas than that of background environment (water) [48].

Several studies have reported that surface oxidation of laser-induced structures is related to the oxygen molecules that exist in air or water which react with the surface during laser processing at high temperatures. During laser processing, the surface was melted which in turn leads to the diffusion of oxygen through the molten material and finally oxidising the treated surface. Furthermore, when the surface particles are evaporated at high fluence, they react with the surrounding oxygen. Then, the redepositing of these oxidised particles in addition to oxidised melted particle would occur [20, 49]. Cui et al [50] mentioned that after heat treating the stainless steel, the oxidation rate depends on the mass transfer rate of oxygen from the surrounding

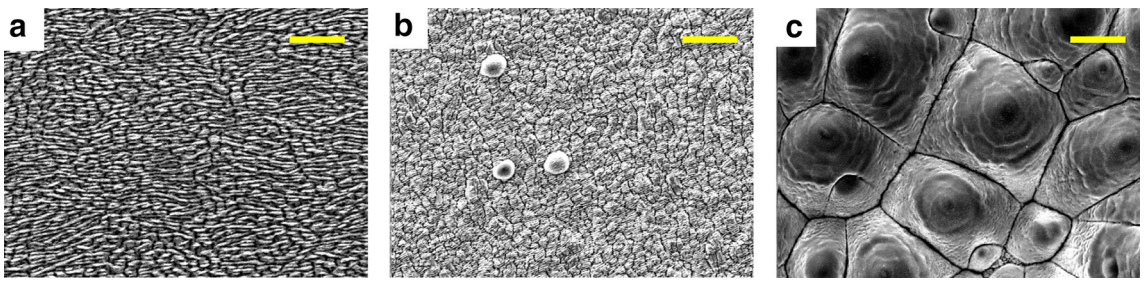

Fig. 9 Surface morphology of ps laser surface textured samples in air using 50 mm/s and **a** 1 pass, **b** 10 pass and **c** 50 pass. The scale bar is 20 µm

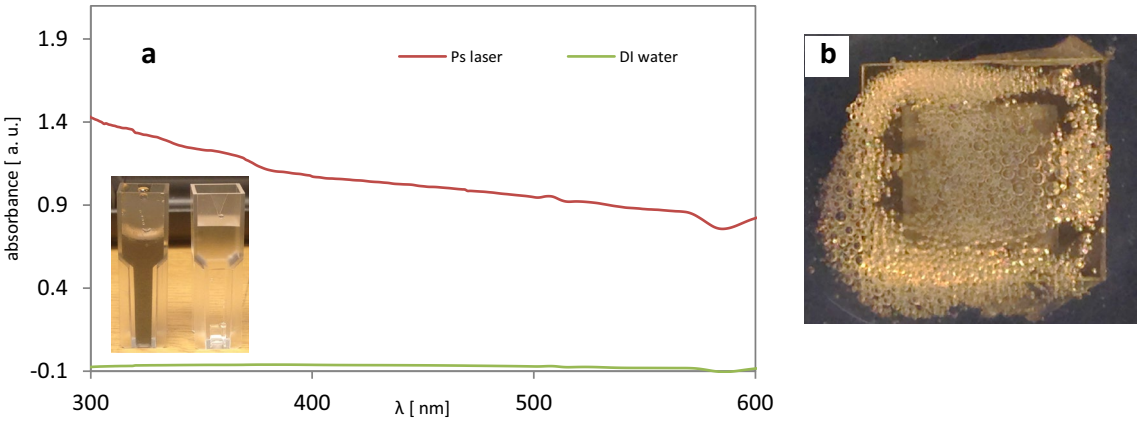

Fig. 10 **a** The absorbance of water before and after laser treatment of the surface at 10 mm/s and one pass of 10 × 10 mm^2 area and **b** bubble formed during laser processing

environment and the diffusion of oxygen into the interior material. The ionised O_2 molecule first preferentially reacts with Cr ions/atoms due to its affinity to oxygen resulting in an ultra-thin layer of Cr_2O_3. Then, Fe_2O_3 is formed due to high temperatures in laser-treated area and high mobility of Fe atom which can diffuse through Cr_2O_3 to react with O forming Fe_2O_3 [50]. There is an agreement between Cui et al. [50] work and our work as shown in the XRD analysis (Fig. 11) that the main oxides were Cr_2O_3 and Fe_2O_3. in addition to a new phase (Ferrite). The phase change was clear in both water and air interaction. However, the oxides were not clear in the case of laser surface texturing in water relating to its low percentage. In water, a significant reduction in the amount of oxygen was noticed than that in the air. The amount of used water was low. Therefore, the amount of oxygen during laser processing in water was limited to the amount of oxygen of this small amount of water resulting in confining the interaction of the molten material with oxygen which in turn affected the final amount of surface oxygen contents. The prevention of redeposition of ablated particle as well as plasma shielding at high laser fluence, which prevents the surface interacting with the surrounding

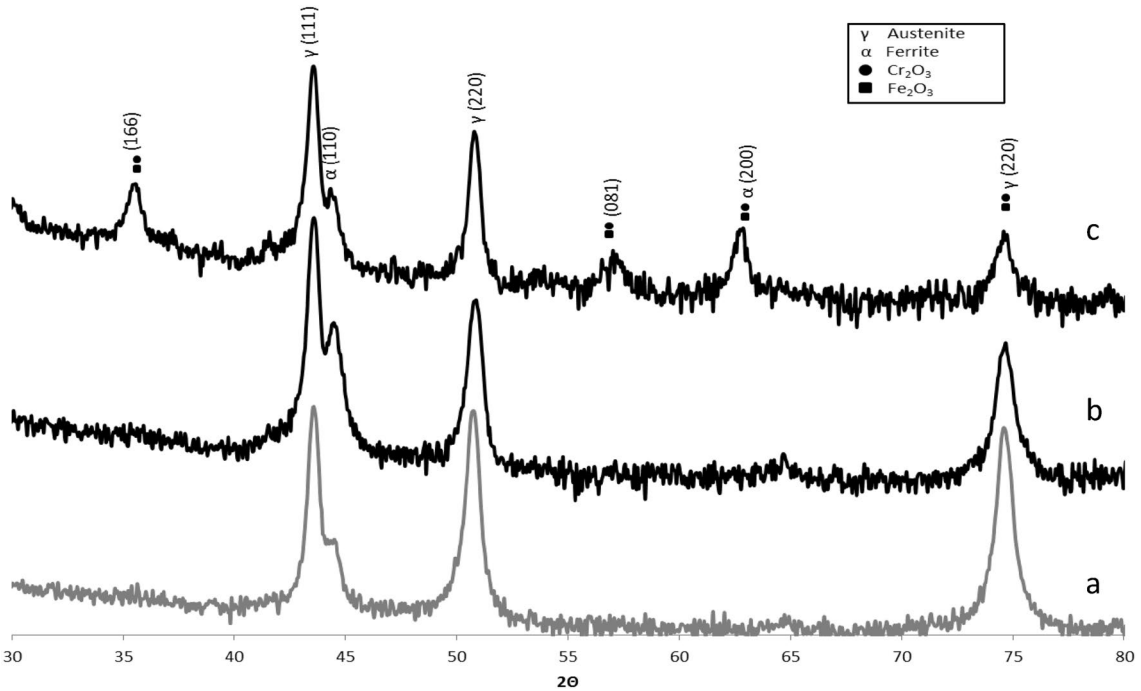

Fig. 11 XRD spectra of **a** as received stainless steel, **b** after ps laser treating stainless steel in water and **c** after ps laser treating stainless steel in the air using 10 mm/s, one pass

environment, might be another reason for low oxygen rate in water [20].

The surface roughness (*Ra*) of as-received stainless steel was 0.011 µm, and in all cases, it was noticed that the surface roughness and surface oxygen content were increased after the laser surface structuring. In this work, changing the wettability of laser surface textures is attributed to the change of surface topography, surface chemistry and surface energy. The textured surfaces was superhydrophilic with small contact angles immediately after laser treatment. However, the wettability of the surfaces after one month of processing, without chemical treatment, was changed to hydrophobic. This is related to the adsorption of organic matter and carbon from atmosphere resulting in decrease in the surface wettability [51]. Without chemical treatment, it was noticed that the surface wettability was increased with increasing surface roughness. The as-received stainless steel surface was hydrophilic with a water contact angle of 80°. The higher wettability of the rougher surfaces can be explained by Wenzel model [52, 53]. The Wenzel equation, $\cos\theta_A = r\cos\theta_Y$, describes the effect of surface roughness on the water droplet, where θ_A is the CA on the rough surface, r is the ratio of the actual solid/liquid contact area to its vertical projected area, and θ_Y is the CA on a flat surface defined by Young's equation. As the roughness (r) increases, the CA decreased reflecting an increase in relative hydrophilicity. It was noticed that the oxidizing level increases with decreasing the speed/increasing the number of scanning passes, which was the same behaviour of changing of surface roughness. This might interpret the behaviour of increasing the wettability with increasing the roughness as it was proved that the amount of adsorbed carbon substances on the surface was dependent on the surface OH group density of metal oxide. This fact indicates that the surface OH (hydroxyl) group density is a major factor governing the adsorption of organic substances from the atmosphere on the surface. The surface OH group density depends on the material and mainly on the negative charge density of the oxygen atom of the film material. In general, the binding energy of electrons in a certain atom is highly influenced by the electronegativity of the atoms directly bond to that particular atom. Therefore, this difference is considered to be related to the electronegativity of metal elements directly bound to the oxygen atom. The OH group density was proved to increase the carbon adsorption with time which affects the wettability stability [54, 55]. Therefore, it can be said that with increasing the scanning times/decreasing the scanning speed, the oxidizing layer increases resulting in increasing the OH group density which affects the wettability to increase. However, the roughness of the surfaces textured in water was lower while its wettability was higher as compared with surfaces treated in air using same parameter. This might be attributed to two reasons. One of them is related to the lower oxidation level compared with that achieved in air which reduced the carbon adsorption and increase the wettability. The second reason is related to smoother surfaces with low aspect ratio (peak to valley ratio) which decreases the contact area between the water droplet and the surface resulting in increasing the wettability. The maximum peak to valleys ratio was 80 µm in air and 11 µm in water. Therefore, it can be said that the surface geometry type and chemistry have a more important role in affecting wettability than surfaces roughness.

For the chemically treated samples, their surface tension was reduced, and the surface chemistry of the samples is similar leaving the surface effects mainly controlled by the surface geometry. It can be seen that all surfaces switched to hydrophobic and CA of surfaces prepared in the air were higher than that prepared in water. Here, with an increase in the roughness, the wettability was decreased as a result of increasing the air trapping between features. The surfaces of higher roughness (for samples prepared using 50 and 10 mm/s speeds) were of lower wettability. This behaviour can be explained by the Cassie state because the surfaces have a large roughness consisting of microstructures combined with submicron and nano-structures. A layer of air was trapped between features preventing wetting of surface [56]. With decreasing the roughness (increasing the speed), the contact angle was slightly decreased resulting in surfaces of high CA with increasing the adhesion of droplet to the surface. As reported by Long et al. [57], these surfaces were characterised as a metastable state based on the Cassie–Wenzel state, which works as a rose petal (Fig. 12). This figure gives an idea of how the surface adhesion changed with changing surface roughness.

During studying of laser-generated microstructures on metal surfaces, it was noticed that after processing, the surface exhibited decreased reflectivity or became completely black in appearance. These findings have also been reported for semiconductor materials such as silicon [58, 59] as well as some other materials [5, 26, 60]. As having been reported on multiple materials, it can be assumed that this effect occurs due to a structural change on the surface. It was reported that the formation of nanoparticles and nano-structures covered the surface which affected the reflectivity and the absorptivity of the material. Indeed, changing the density of nanoparticle aggregation affects the reflectivity [17]. Here, with reducing scanning speed/increasing the scanning passes, the redepositing particles was increased, and the generation of surface of micro/nano-structure was clearer, which aids the multiple reflections inside the structure to decrease the final reflectivity of the surface. However, in water, the surface was smoother with less redeposited particles resulting in a higher light reflectivity.

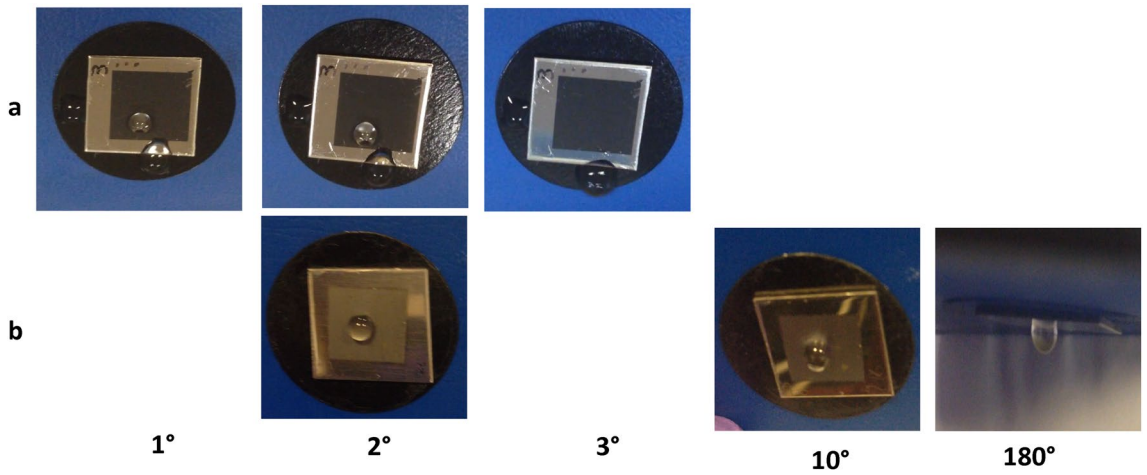

Fig. 12 Changing the state of laser-textured surfaces after reducing surface tension by chemical treatment **a** Cassie state (air, 50 mm/s, one pass), **b** metastable state (water, 500 mm/s, one pass)

5 Conclusions

In this work, the characteristics of surface texturing using short (ps) pulse lasers in air and water were investigated. The formation of different structures was mainly due to thermal processes. Different micro/nano-structures were generated on the stainless steel surface by manipulating the processing parameters. There was a difference in structures generated in air from that in water. Structures generated in water were shallower with lower roughness and smaller features with much less deposited nanoparticles. The surface oxidation was high in the air as well as the surface water contact angles. The surfaces prepared in the air were of lower reflectivity compared with that prepared in water. Using water as a processing medium allowed of generating smoother, finer micro structures giving lower oxidising surfaces comparing with that generated in air. Indeed, using a high power ps laser as a texturing tool would provide the possibility of generating different structures of different properties, which may be tailored for different applications.

Acknowledgements The authors acknowledge Iraqi Ministry of Higher Education and Scientific Research (MOHESR) for the financial support of Fatema Rajab's PhD research.

References

1. H.-W. Chang, Y.-C. Tsai, C.-W. Cheng, C.-Y. Lin, Y.-W. Lin, T.-M. Wu, J. Colloid Interface Sci. **360**, 305–308 (2011)
2. R. Buividas, P.R. Stoddart, S. Juodkazis, Annalen der Physik 524 (2012)
3. I. Etsion, Tribol. Lett. **17**, 733–737 (2004)
4. X. Wang, K. Kato, K. Adachi, Tribol T **45**, 294–301 (2002)
5. J. Long, P. Fan, M. Zhong, H. Zhang, Y. Xie, C. Lin, Applied Surface Sci. **311**, 461–467 (2014)
6. J. Long, L. Pan, P. Fan, D. Gong, D. Jiang, H. Zhang, L. Li, M. Zhong, Langmuir **32**, 1065–1072 (2016)
7. R. Jagdheesh, Langmuir **30**, 12067–12073 (2014)
8. S. Perni, P. Prokopovich, Soft Matter **9**, 1844–1851 (2013)
9. A. Cunha, O.F. Zouani, L. Plawinski, A.M.B. do Rego, A. Almeida, R. Vilar, M.C. Durrieu, Nanomedicine-Uk 10, 725–739 (2015)
10. A. Cunha, A.-M. Elie, L. Plawinski, A.P. Serro, A.M.B. do Rego, A. Almeida, M.C. Urdaci, M.-C. Durrieu, R. Vilar, Applied Surface Science 360, 485–493 (2016)
11. S. Schlie, E. Fadeeva, J. Koch, A. Ngezahayo, B.N. Chichkov, J. Biomater. Appl. **25**, 217–233 (2010)
12. A. Alshehri, S. Hadjiantoniou, R. Hickey, Z. Al-Rekabi, J. Harden, A. Pelling, V. Bhardwaj, Biomed. Mater. **11**, 015014 (2016)
13. E. Fadeeva, V.K. Truong, M. Stiesch, B.N. Chichkov, R.J. Crawford, J. Wang, E.P. Ivanova, Langmuir **27**, 3012–3019 (2011)
14. E. Fadeeva, A. Deiwick, B. Chichkov, S. Schlie-Wolter, Interface Focus **4**, 20130048 (2014)
15. Y. Guan, F. Luo, G. Lim, M. Hong, H. Zheng, B. Qi, Mater Design **78**, 19–24 (2015)
16. K.-H. Leitz, B. Redlingshöfer, Y. Reg, A. Otto, M. Schmidt, Physics Procedia **12**, 230–238 (2011)
17. P. Fan, M. Zhong, L. Li, T. Huang, H. Zhang, Opt. Express **21**, 11628–11637 (2013)
18. N. Muhammad, L. Li, Appl. Phys. A **107**, 849–861 (2012)
19. Y.Q. Zhou, T.M. Shao, L. Yin, Laser Phys. **19**, 1061–1066 (2009)
20. S. Razi, K. Madanipour, M. Mollabashi, Optics Laser Technol. **80**, 237–246 (2016)
21. D. Fried, N. Ashouri, T. Breunig, R. Shori, Lasers Surg. Med. **31**, 186–193 (2002)
22. M.S. William, M. Jyotirmoy, Steen Springer-Verlag, London, Berlin, Heidelberg 3, 408 (2010)
23. J. Eichstädt, G. Römer, A. Huis, Appl. Surface Sci. **264**, 79–87 (2013)
24. T.T. Dai Huynh, A. Petit, N. Semmar, Appl. Surface Sci. **302**, 109–113 (2014)
25. J.V. Obona, V. Ocelík, J. Skolski, V. Mitko, G. Römer, A. Huis, J.T.M. De Hosson, Appl. Surface Sci. **258**, 1555–1560 (2011)
26. M.H. Dar, R. Kuladeep, V. Saikiran, Appl. Surface Sci. **371**, 479–487 (2016)
27. K.T. Ahmmed, E.J.Y. Ling, P. Servio, A.-M. Kietzig, Opt. Laser Eng. **66**, 258–268 (2015)

28. A.M. Emelyanenko, F.M. Shagieva, A.G. Domantovsky, L.B. Boinovich, Appl. Surface Sci. **332**, 513–517 (2015)
29. B. Liu, W. Wang, G. Jiang, X. Mei, K. Wang, J. Wang, J. Nanomater. **2013**, 11-11 (2013)
30. J. Lehr, A.-M. Kietzig, Opt. Laser Eng. **57**, 121–129 (2014)
31. A. Pena, Z. Wang, D. Whitehead, R. Lloyd, L. Li, J. Phys. D Appl. Phys. **43**, 115302 (2010)
32. B. Liu, G. Jiang, W. Wang, X. Mei, K. Wang, J. Cui, J. Wang, Opt Laser Eng **78**, 55–63 (2016)
33. A. Gökhan Demir, V. Furlan, N. Lecis, B. Previtali, Biointerphases **9**, 029009 (2014)
34. D. Kam, S. Bhattacharya, J. Mazumder, J. Micromech. Microeng. **22**, 105019 (2012)
35. Y. Li, Z. Cui, W. Wang, C. Lin, H.-L. Tsai, Appl. Surface Sci. **324**, 775–783 (2015)
36. B. Nayak, M. Gupta, K. Kolasinski, Appl. Phys. A **90**, 399–402 (2008)
37. R. Lloyd, A. Abdolvand, M. Schmidt, P. Crouse, D. Whitehead, Z. Liu, L. Li, Appl. Phys. A **93**, 117–122 (2008)
38. A. Abdolvand, R.W. Lloyd, M.J. Schmidt, D.J. Whitehead, Z. Liu, L. Li, Appl. Phys. A **95**, 447–452 (2009)
39. C. Albu, A. Dinescu, M. Filipescu, M. Ulmeanu, M. Zamfirescu, Appl. Surface Sci. **278**, 347–351 (2013)
40. E. Golosov, V.I.i. Emel'yanov, A.A. Ionin, Y.R. Kolobov, S.I. Kudryashov, A.E. Ligachev, Y.N. Novoselov, L.V. Seleznev, D.V.e. Sinitsyn, Jetp Lett + 90, 107–110 (2009)
41. S. Bashir, M.S. Rafique, A. Ajami, W. Husinsky, Appl. Phys. A **113**, 673–681 (2013)
42. X. Liu, D. Du, G. Mourou, Ieee J Quantum Elect. **33**, 1706–1716 (1997)
43. N. Nedialkov, S. Imamova, P. Atanasov, J. Phys. D Appl. Phys. **37**, 638 (2004)
44. S. Juodkazis, H. Okuno, N. Kujime, S. Matsuo, H. Misawa, Appl. Phys. A Mater. Sci. Process. **79**, 1555–1559 (2004)
45. S. Moradi, S. Kamal, P. Englezos, S.G. Hatzikiriakos, Nanotechnology **24**, 415302 (2013)
46. G. Daminelli, J. Krüger, W. Kautek, Thin Solid Films **467**, 334–341 (2004)
47. M.H. Mahdieh, M. Akbari, Jafarabadi. Appl. Phys. A **116**, 1211–1220 (2014)
48. M. Mahdieh, M.A. Jafarabadi, Appl. Phys. A **116**, 1211–1220 (2014)
49. C.Y. Cui, X.G. Cui, X.D. Ren, M.J. Qi, J.D. Hu, Y.M. Wang, Appl. Surf. Sci. **305**, 817–824 (2014)
50. C. Cui, X. Cui, X. Ren, M. Qi, J. Hu, Y. Wang, Appl. Surf. Sci. **305**, 817–824 (2014)
51. D.V. Ta, A. Dunn, T.J. Wasley, R.W. Kay, J. Stringer, P.J. Smith, C. Connaughton, J.D. Shephard, Applied Surface Science 357, Part A, 248–254 (2015)
52. R.N. Wenzel, Ind. Eng. Chem. **28**, 988–994 (1936)
53. R.N. Wenzel, J. Phys. Chem. **53**, 1466–1467 (1949)
54. S. Takeda, M. Fukawa, Y. Hayashi, K. Matsumoto, Thin Solid Films **339**, 220–224 (1999)
55. S. Takeda, M. Fukawa, Thin Solid Films **444**, 153–157 (2003)
56. Z. Cheng, M. Du, H. Lai, N. Zhang, K. Sun, Nanoscale **5**, 2776–2783 (2013)
57. J. Long, P. Fan, D. Gong, D. Jiang, H. Zhang, L. Li, M. Zhong, ACS Appl. Mater. Interfaces. **7**, 9858–9865 (2015)
58. C. Wu, C. Crouch, L. Zhao, J. Carey, R. Younkin, J. Levinson, E. Mazur, R. Farrell, P. Gothoskar, A. Karger, Appl. Phys. Lett. **78**, 1850–1852 (2001)
59. A.Y. Vorobyev, C. Guo, Appl. Surf. Sci. **257**, 7291–7294 (2011)
60. H. Huang, L.-M. Yang, S. Bai, J. Liu, Appl. Opt. **54**, 324–333 (2015)